



Article

Facile Synthesis of S/Ti₃C₂T_x Mxene@Se Cathode for High-Sulfur-Loading Lithium–Sulfur Batteries

Yupu Shi ¹, Jianbin Xu ², Xian Du ¹, Yi Zhang ³ , Fan Zhao ¹, Ziwei Tang ¹, Le Kang ^{1,*} and Huiling Du ^{1,*}

¹ College of Materials Science and Engineering, Xi'an University of Science and Technology, Xi'an 710054, China; forlisser@xust.edu.cn (Y.S.); dx@xust.edu.cn (X.D.); 21211225041@stu.xust.edu.cn (F.Z.); 21211025014@stu.xust.edu.cn (Z.T.)

² Tianjin Sanyuan Electric Power Group Co., Ltd., Tianjin 300010, China; jsyxjb@163.com

³ School of Energy Sciences and Engineering, Nanjing Tech University, Nanjing 211816, China; zhangy@njtech.edu.cn

* Correspondence: kangle20140805@126.com (L.K.); hldu@xust.edu.cn (H.D.)

Abstract: Lithium–sulfur batteries (LSBs) are gaining much attention because they offer a much higher theoretical energy density compared to traditional lithium-ion batteries. However, the cycling performance of LSBs with high sulfur mass loading is poor due to the shuttle effect, limiting the practical application of LSBs. In this work, a unique porous sulfur/Ti₃C₂T_x Mxene@selenium (S/Ti₃C₂T_x@Se) cathode of a LSB is synthesized by a simple hydrothermal method to address these challenges. In this composite, Ti₃C₂T_x forms a conductive framework and Se is tightly anchored on the framework. The Se inhibits the agglomeration of Ti₃C₂T_x and prevents the collapse of Ti₃C₂T_x. The S/Ti₃C₂T_x@Se composite can adsorb lithium polysulfides (LiPSs) and suppresses the shuttle effect and volume changes during cycling, improving the cycling stability of LSBs with high S loading. A high capacity of 812.2 mAh g⁻¹ at 0.1 C with 5.0 mg cm⁻² sulfur mass loading after 100 cycles is obtained. This work could inspire further research into high-performance S host materials for high-S-loading LSBs.

Keywords: selenium; Ti₃C₂T_x Mxene; cathode; lithium–sulfur batteries; high loading



Citation: Shi, Y.; Xu, J.; Du, X.; Zhang, Y.; Zhao, F.; Tang, Z.; Kang, L.; Du, H. Facile Synthesis of S/Ti₃C₂T_x Mxene@Se Cathode for High-Sulfur-Loading Lithium–Sulfur Batteries. *Batteries* **2024**, *10*, 430. <https://doi.org/10.3390/batteries10120430>

Academic Editor: Marco Giorgetti

Received: 15 October 2024

Revised: 19 November 2024

Accepted: 27 November 2024

Published: 3 December 2024



Copyright: © 2024 by the authors. Licensee MDPI, Basel, Switzerland. This article is an open access article distributed under the terms and conditions of the Creative Commons Attribution (CC BY) license (<https://creativecommons.org/licenses/by/4.0/>).

1. Introduction

The depletion of fossil fuels and environmental pollution have created an urgent demand for the development of renewable energy. Solar cells, lithium-ion batteries, and sodium-ion batteries are essential for sustainable energy [1–4]. Among these, lithium-ion batteries stand out for their exceptional performance, particularly in consumer electronics, flexible devices, and transportation [5–12]. However, one limitation of lithium-ion batteries is their limited energy density. Lithium–sulfur batteries (LSBs) are gaining much attention because they offer a much higher theoretical energy density (2600 Wh kg⁻¹) compared to traditional lithium-ion batteries. The theoretical specific capacity of sulfur is 1675 mAh g⁻¹, which also outpaces many current cathode materials [13–18]. However, there are some issues for LSBs which need to be overcome, including (i) the dissolution of intermediate products (Li₂S_n, 4 ≤ n ≤ 8) which is named the “shuttle effect”; (ii) the low electrical conductivity of sulfur; and iii) the huge volume change during cycling [19–22]. These imperfections cause poor electrochemical performance, such as low specific capacity, low Coulombic efficiency, and rapid capacity fading. So far, many strategies have been developed to address LSB issues, such as developing porous host materials for sulfur [23–25], separator modification [26–28], and electrolyte engineering [29]. The most common and effective method is to design porous S host materials to enable a suppressed shuttle effect.

In recent years, a novel two-dimensional material (Ti₃C₂T_x Mxene) has been widely applied in energy storage owing to the controlled synthetic method, excellent conductivity

and abundant functional surface groups [30–34]. Moreover, $\text{Ti}_3\text{C}_2\text{T}_x$ Mxene exhibits significant potential to mitigate the shuttle effect and accommodate the sulfur volume expansion during lithiation owing to its layered architecture and large pore volume. In a recent study, Wang et al. [35] easily prepared S/ $\text{Ti}_3\text{C}_2\text{T}_x$ Mxene by a hydrothermal method. The sulfur nanoparticles are uniformly distributed within the $\text{Ti}_3\text{C}_2\text{T}_x$ layers, which is crucial to the electrochemical performance of LSBs. The $\text{Ti}_3\text{C}_2\text{T}_x$ ensures that sulfur, which has low intrinsic conductivity, is closely integrated with a highly electrically conductive $\text{Ti}_3\text{C}_2\text{T}_x$. This structure leads to enhanced electrochemical performance (a high initial capacity of 1277 mAh g^{-1} and a stable capacity of 1059 mAh g^{-1} at 0.5 C after 100 cycles).

Although the S/ $\text{Ti}_3\text{C}_2\text{T}_x$ Mxene cathode showed improved electrochemical performance, it possessed low areal sulfur loading ($<3 \text{ mg cm}^{-2}$) due to the $\text{Ti}_3\text{C}_2\text{T}_x$ Mxene creating irreversible agglomerates via the van der Waals force, which limited its practical application. According to the commercial requirement, LSB cathodes must have a high sulfur loading ($>4 \text{ mg cm}^{-2}$). However, high-sulfur-loading cathodes suffer from a severe shuttle effect. Utilization of conductive coatings to prevent the severe shuttle effect has been demonstrated as an effective strategy to enhance the cycling stability of LSBs with high sulfur loading. Yu et al. reported a PDA-coated $\text{Ti}_3\text{C}_2\text{T}_x$ Mxene/sulfur cathode which showed excellent cycling stability (556 mAh g^{-1} after 330 cycles at 0.5 C) with 4.4 mg cm^{-2} sulfur loading [36]. Se possesses high electrical conductivity and greatly enhances electron transport, holding great promise for a $\text{Ti}_3\text{C}_2\text{T}_x$ Mxene/sulfur cathode. Thus, we have prepared a unique porous sulfur/ $\text{Ti}_3\text{C}_2\text{T}_x$ Mxene@selenium (S/ $\text{Ti}_3\text{C}_2\text{T}_x@\text{Se}$) cathode. The Se inhibits the agglomeration of $\text{Ti}_3\text{C}_2\text{T}_x$. As a result, the S/ $\text{Ti}_3\text{C}_2\text{T}_x@\text{Se}$ composite shows a high capacity of 812.2 mAh g^{-1} after 100 cycles at 0.1 C with 5.0 mg cm^{-2} sulfur mass loading.

2. Experimental

2.1. Preparation of $\text{Ti}_3\text{C}_2\text{T}_x/\text{S}@\text{Se}$

A total of 40 mL HF (Sigma-Aldrich, 48%, St. Louis, MO, USA) was added into a plastic Erlenmeyer flask, and a PTFE-coated stirring bar was used. Then, 0.5 g MAX precursor (Ti_3AlC_2) (Nanjing XFNANO Materials Tech Co., Ltd., Nanjing, China) was added in and the mixture was stirred for 96 h at room temperature. After etching, the sample was washed with DI water until the supernatant reached a pH above 6 and then dried for 24 h at 80 °C in an oven to obtain $\text{Ti}_3\text{C}_2\text{T}_x$ Mxene. The sulfur was encapsulated into $\text{Ti}_3\text{C}_2\text{T}_x$ Mxene and Se via a hydrothermal process. Typically, the $\text{Ti}_3\text{C}_2\text{T}_x$ Mxene powder was added into a 7:1 (volume ratio) water/ethanol solution, followed by ultrasonic treatment for 1 h. The purpose of the ultrasonic treatment was to promote dispersion of the $\text{Ti}_3\text{C}_2\text{T}_x$ Mxene in the solution, ensuring that the mixture was homogeneous. Carbon disulfide (CS_2) (Sigma-Aldrich, St. Louis, MO, USA) was used as a solvent to dissolve the sulfur and selenium powders; the solution contained 600 mg of sulfur in 10 mL CS_2 and 120 mg of selenium in 2 mL CS_2 . Subsequently, the S and Se solutions were added into the above mixture, then treated in an ultrasonic grinder for 0.1 h to disperse S and Se in the mixture. The mixture was transferred to a Teflon-lined autoclave, which was then heated to 220 °C (close to selenium's melting point) for 12 h. In this process, the S powder was first melted and filled into the layers of $\text{Ti}_3\text{C}_2\text{T}_x$ Mxene. Then, the Se was melted and coated on the surface of the S/ $\text{Ti}_3\text{C}_2\text{T}_x$ composite when the reaction temperature reached Se's melting point. The mixture was transferred to a Teflon-lined autoclave, which was then heated to 220 °C (close to selenium's melting point) for 12 h. The product was washed three times with distilled water to remove any residual products or unreacted materials. The final step involved drying the product in an oven at 80 °C for 24 h. The schematic of preparation of the S/ $\text{Ti}_3\text{C}_2\text{T}_x@\text{Se}$ composite is shown in Figure 1.

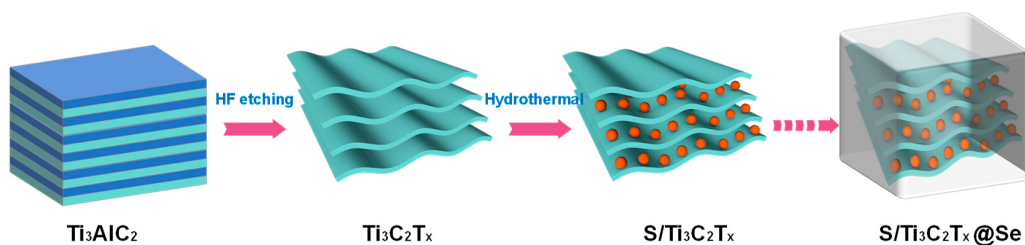


Figure 1. Schematic of preparation of S/Ti₃C₂T_x@Se composite.

2.2. Characterizations

The structure of samples was characterized by X-ray diffraction (XRD) (Rigaku Mini-Flexll, Rigaku Corporation, Tokyo, Japan). Scanning electron microscopy (SEM) (JEOL JSM-7800F Field Emission, Manufacturer JEOL Ltd., Tokyo, Japan) at 5 kV and corresponding energy dispersive spectroscopy (EDX) were used to analyze the samples' morphologies. The Raman spectra (632 nm) were collected with a RE01 (Renishaw Inc., London, UK). Thermogravimetric analysis (TGA) measurements were carried out by a Mettler Toledo TGA/SDTA 851 (Zurich, Switzerland).

2.3. Electrochemical Tests

The sulfur cathode was fabricated as follows: 60 wt% active material, 30 wt% conductive carbon black, and 10 wt% polytetrafluoroethylene (PTFE) were mixed to form a paste, which was subsequently pressed onto nickel foam. The electrolyte consisted of 1 M lithium bis(trifluoromethane sulfonyl)imide dissolved in a 1:1 (volumetric ratio) 1,3-dioxolane/dimethoxyethane with 1 wt% lithium nitrate. The separator was Celgard 2400 (LLC-Headquarters & Charlotte Manufacturing Facility, North Carolina, USA). Lithium foil served as the counter electrode. The assembly of the coin cells was carried out in a glove box filled with Ar. Galvanostatic discharge and charge tests were conducted using a Land CT2001 battery tester (Wuhan Land Electronic Co. Ltd., Wuhan, Hubei, China), operating within a voltage range of 1.6 to 2.8 V versus Li/Li⁺. Additionally, cyclic voltammetry (CV) was performed at a scanning rate of 0.1 mV s⁻¹, also covering the 1.6 to 2.8 V potential range, using a PGSTAT 302N electrochemical station (Wuhan Land Electronic Co., Ltd., Wuhan, Hubei, China).

3. Results and Discussion

Figure 2a presents the XRD patterns of the MAX phase precursor (Ti₃AlC₂) and Mxene product (Ti₃C₂T_x). The MAX exhibits strong peaks at 2θ values of 9.6°, 19.1°, 34.1°, 36.9°, 38.9°, 42.0°, 45.0°, 48.5°, and 52.5°, corresponding to the (002), (004), (101), (103), (104), (105), (106), (107), and (108) planes of Ti₃AlC₂ (JCPDS No. 52-0875) [37], respectively. And the diffraction peaks are sharp, indicating high crystallinity. After HF etching, however, the XRD pattern shows a reduction in peak intensity, signifying a decrease in crystallinity. In addition, the diffraction peak corresponding to the (002) plane shows an obvious shift to a lower angle, and the peaks at the 2θ values of 36.9°, 38.9°, and 42.0° are no longer present. These changes suggest the successful removal of Al atomic layers through HF etching, resulting in an increased d-spacing within the Ti₃C₂T_x layers. The Raman spectra (Figure 2b) prove these observations, with peaks located at 161 cm⁻¹, 242 cm⁻¹, 281 cm⁻¹, 442 cm⁻¹, and 621 cm⁻¹ [35]. After etching, the peaks at 161 cm⁻¹, 242 cm⁻¹, and 281 cm⁻¹ are nearly absent, indicating significant structural changes during the etching process. Figure 2c-f are SEM images of Ti₃AlC₂ and Ti₃C₂T_x. Figure 2c displays the dense structure of Ti₃AlC₂, while Figure 2e-f illustrate the multilayered structure of Ti₃C₂T_x after etching. This layered morphology facilitates the uniform distribution and anchoring of nanoparticles between the layers.

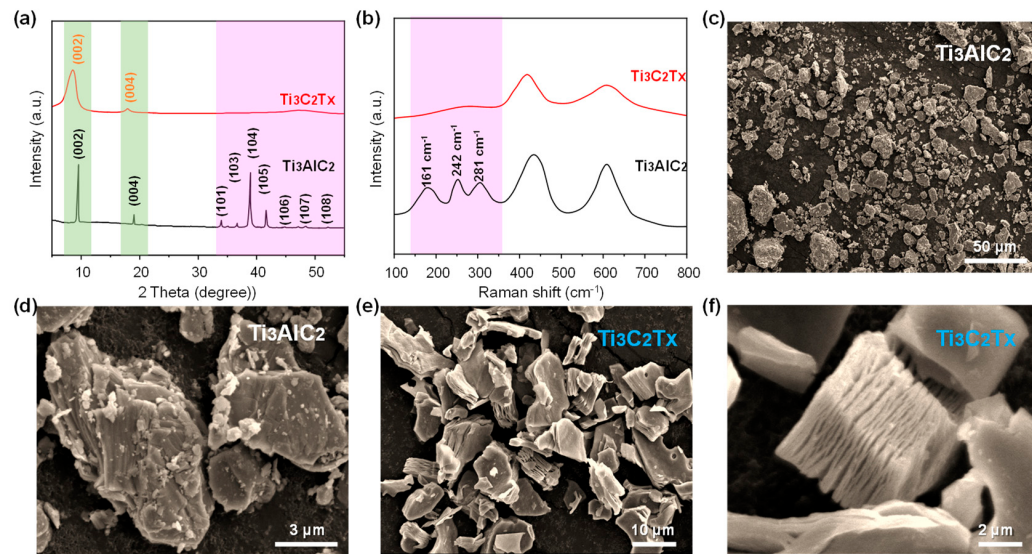


Figure 2. (a) XRD patterns of MAX and Mxene. (b) Raman patterns of MAX and Mxene. (c,d) SEM images of MAX. (e,f) SEM images of Mxene.

The S/Ti₃C₂T_x composite was synthesized using a hydrothermal reaction. To assess the sulfur content, TGA was conducted under a nitrogen atmosphere. The TGA results are illustrated in Figure 3a. There are two weight-loss steps. In the initial step, from room temperature to 110 °C, the weight decreases by 0.62%, resulting from the evaporation of surface-bound water and residual HF. Between 110 °C and 300 °C, a major weight reduction of 67.5% occurs, corresponding to the sulfur loss from the S/Ti₃C₂T_x composite. Thus, the sulfur content was quantified to be 67.5 wt%. Figure 3b displays XRD patterns of sulfur and the S/Ti₃C₂T_x composite. There is a strong resemblance between sulfur and the S/Ti₃C₂T_x composite due to the high content of sulfur in Ti₃C₂T_x. Figure 3c,d present SEM images of the S/Ti₃C₂T_x composite, highlighting that sulfur nanoparticles are uniformly dispersed between the Ti₃C₂T_x layers. The hydrothermal reaction is a simple synthesis technique performed under relatively moderate conditions. By this method, we were able to regulate the interaction between Ti₃C₂T_x and sulfur in solution, ensuring uniform sulfur nanoparticle distribution both within the layers and on the surface of the Ti₃C₂T_x.

Figure 4 illustrates the morphology and structure of the S/Ti₃C₂T_x@Se composite. Figure 4a presents the TGA curve of the S/Ti₃C₂T_x@Se composite in a nitrogen atmosphere and shows a three-step weight loss. In the first step, from room temperature to 110 °C, the observed weight loss is due to the evaporation of surface-bound water. The second step, occurring between 110 °C and 200 °C, shows a major weight reduction caused by the sulfur loss from the composite. In the third step, above 200 °C, the weight loss is attributed to the evaporation of Se. Based on these results, the sulfur content was measured at 47.7 wt%, while the selenium content was found to be 6.1 wt%. Due to the relatively low content of Se, the characteristic diffraction peak for Se cannot be observed in the XRD pattern of the S/Ti₃C₂T_x@Se composite (Figure 4b). Figure 4d–f are SEM images of the S/Ti₃C₂T_x@Se composite. Figure 4d shows the S/Ti₃C₂T_x@Se composite's ball-like structure. From Figure 4e, we can observe that the S/Ti₃C₂T_x@Se composite is wrapped by a thin layer of Se. Figure 4f is a cross-sectional SEM image of the S/Ti₃C₂T_x@Se composite. We can observe that the S nanoparticles are fixed in Ti₃C₂T_x layers, and a thin layer of Se is wrapped over the S/Ti₃C₂T_x composite. Figure 4g–j are SEM–EDX mapping images of the S/Ti₃C₂T_x@Se composite. The yellow, red, green, and blue parts represent the Ti, C, S, and Se. We can observe that Se uniformly wraps over the S/Ti₃C₂T_x composite.

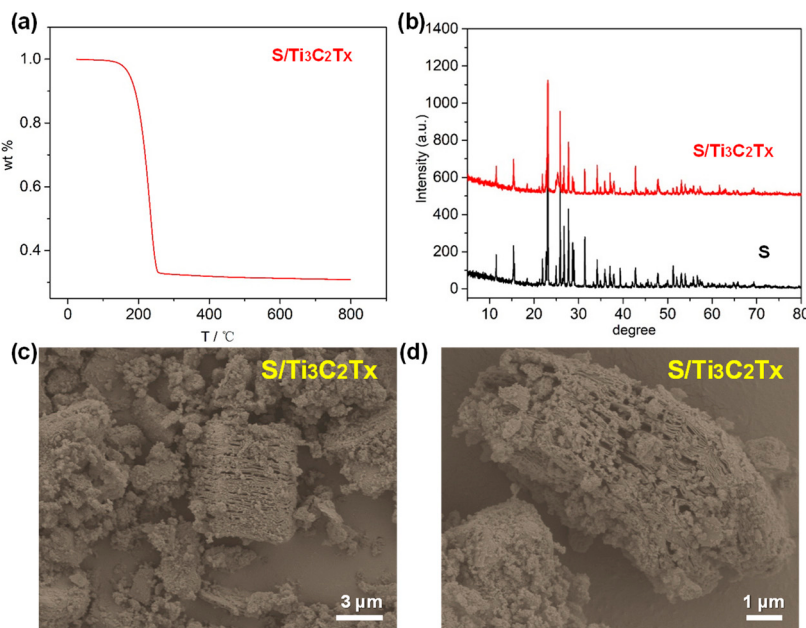


Figure 3. (a) TGA of S/Ti₃C₂T_x composite. (b) XRD patterns of S and S/Ti₃C₂T_x composite. (c,d) SEM images of S/Ti₃C₂T_x composite.

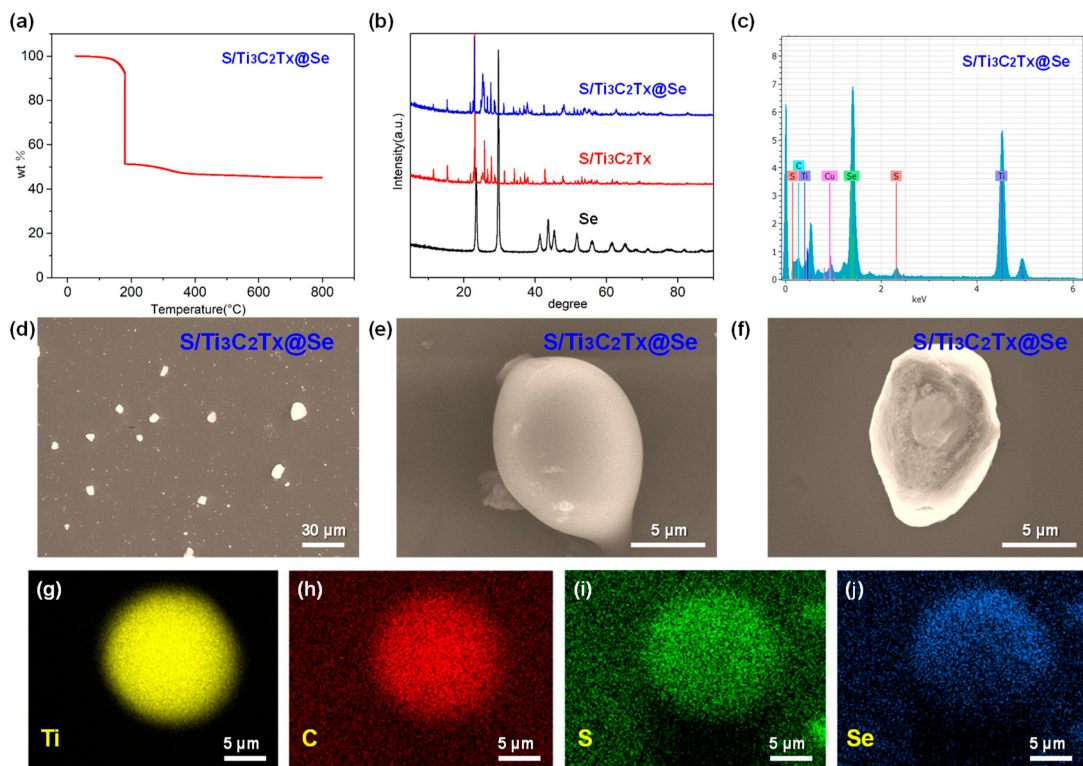


Figure 4. (a) TGA of S/Ti₃C₂T_x@Se composite. (b) XRD patterns of S, S/Ti₃C₂T_x composite and S/Ti₃C₂T_x@Se composite. (c) SEM-EDX pattern of S/Ti₃C₂T_x@Se composite. (d–f) SEM images of S/Ti₃C₂T_x@Se composite. (g–j) SEM-EDX mapping images of S/Ti₃C₂T_x@Se composite.

Figure 5 presents the S/Ti₃C₂T_x@Se composite's electrochemical performance. Figure 5a shows the CV curves of the S/Ti₃C₂T_x@Se composite in which two reduction peaks at 1.72 V and 2.18 V are associated with the lithiation process, while three oxidation peaks at 1.83 V, 2.32 V, and 2.51 V correspond to the delithiation process. It is notable that the S/Ti₃C₂T_x@Se composite has a higher oxidation peak current and reduction peak current compared to the

other S/Ti₃C₂T_x composite [35], which indicates that the Se can improve the conductivity of the S cathode material. The galvanostatic charge–discharge curves (Figure 5b) exhibit two distinct plateaus at 1.70 V and 2.13 V during discharge and three plateaus at 1.80 V, 2.28 V, and 2.50 V during charge. There is a differentiation of the redox peak and plateau potentials which is due to the complex side reactions in the initial cycles. Figure 5c illustrates the cycling performance of both the S/Ti₃C₂T_x composite and the S/Ti₃C₂T_x@Se composite at 0.1 C. For the S/Ti₃C₂T_x composite, the initial reversible capacity is 892.9 mAh g⁻¹, which declines rapidly to 225.3 mAh g⁻¹ after 100 cycles. In contrast, the S/Ti₃C₂T_x@Se composite starts with an initial reversible capacity of 1069.7 mAh g⁻¹ and maintains a stable reversible capacity of 812.2 mAh g⁻¹ after 100 cycles. The capacity retention of the S/Ti₃C₂T_x@Se composite is as high as 75.9%, which is much higher than that of S/Ti₃C₂T_x (25.2%). The cycling performance of the S/Ti₃C₂T_x@Se cathode is better than that of the previously reported S-based cathode (Table 1) [35,38–42]. With a multilayered 2D structure, Ti₃C₂T_x as a host material can buffer the volume expansion. However, the shuttle effect of LiPSs cannot be avoided by Ti₃C₂T_x at high S mass loading. Thus, the S/Ti₃C₂T_x cathode shows a low capacity retention. In the S/Ti₃C₂T_x@Se composite, Ti₃C₂T_x forms a conductive framework and Se is tightly anchored on the framework. The Se inhibits the agglomeration of Ti₃C₂T_x and prevents the collapse of Ti₃C₂T_x. The S/Ti₃C₂T_x@Se composite can adsorb lithium polysulfides (LiPSs) and suppresses the shuttle effect and volume changes during cycling, improving the cycling stability of LSBs. And Ti₃C₂T_x and Se possess high electrical conductivity and greatly enhance the electron transport [43–49], enabling the S/Ti₃C₂T_x@Se composite to exhibit an ideal rate performance. It exhibits high average capacities at different current densities, with average discharge specific capacities at current densities of 0.1–2.0 C of 881.2, 717.9, 603.1, 441.1, and 386.5, and 213.8 mAh g⁻¹, respectively. When the current density was returned to 0.1 C, the discharge specific capacity also recovered to 821.2 mAh g⁻¹.

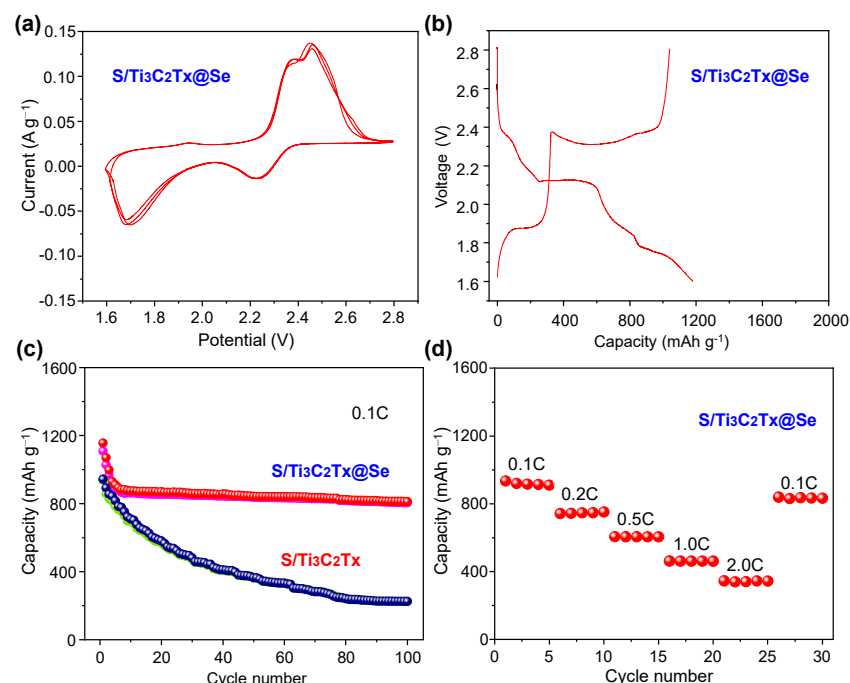


Figure 5. (a) CV of S/Ti₃C₂T_x@Se composite at the scan rate of 0.1 mV s⁻¹. (b) Galvanostatic charge/discharge curves of S/Ti₃C₂T_x@Se composite at 0.1 C at 1.6–2.8V. (c) Cycling performance of S/Ti₃C₂T_x@Se composite and S/Ti₃C₂T_x composite at 0.1 C. (d) Rate performance of S/Ti₃C₂T_x@Se composite.

Table 1. Comparison of the cycling performance of the S/Ti₃C₂T_x@Se composite and previously reported S-based cathode.

Material	S Mass Loading (mg cm ⁻²)	Cycling Times	Capacity (mAh g ⁻¹)	Ref.
HEMN/S@GR	1.0	100	695	[38]
PPY@CMK-8/S	1.0	100	860	[39]
S@NG	0.8	100	830	[40]
S/ACF	5.1	100	750	[41]
graphene–sulfur	3.0	100	600	[42]
S/Ti ₃ C ₂ T _x	3.0	100	578	[35]
S/Ti ₃ C ₂ T _x @Se	5.0	100	812.2	This work

4. Conclusions

In this work, we easily prepared a unique porous sulfur/Ti₃C₂T_x Mxene@selenium (S/Ti₃C₂T_x@Se) cathode of a LSB by a hydrothermal method. SEM images showed that S nanoparticles are homogeneously embedded in the Ti₃C₂T_x sheets and that film-like Se wraps the S/Ti₃C₂T_x. Because of Mxene’s highly electrically conductive multilayered 2D structure with Se coatings, the S/Ti₃C₂T_x@Se composite showed improved reversible specific capacity and cycling performance at high sulfur mass loading. Its initial reversible capacity is 1069.7 mAh g⁻¹ and it retains an 812.2 mAh g⁻¹ capacity after 100 cycles at 0.1 C with a high capacity retention of 75.9% at a sulfur mass loading of 5.0 mg cm⁻². These results suggest that a novel cathode material with good electrochemical performance can be used in LSBs.

Author Contributions: Conceptualization, X.D.; Methodology, L.K.; Validation, F.Z.; Formal analysis, J.X. and Z.T.; Investigation, J.X.; Writing—original draft, Y.S.; Writing—review & editing, H.D.; Supervision, Y.Z. All authors have read and agreed to the published version of the manuscript.

Funding: This research received no external funding.

Data Availability Statement: The original contributions presented in the study are included in the article, further inquiries can be directed to the corresponding author.

Conflicts of Interest: Author Jianbin Xu was employed by the company Tianjin Sanyuan Electric Power Group Co., Ltd. The remaining authors declare that the research was conducted in the absence of any commercial or financial relationships that could be construed as a potential conflict of interest.

References

- An, T.; Zhang, Y.; Wen, J.; Dong, Z.; Du, Q.; Liu, L.; Wang, Y.; Xing, G.; Zhao, X. Multi-Level Pyramidal Microstructure-Based Pressure Sensors with High Sensitivity and Wide Linear Range for Healthcare Monitoring. *ACS Sens.* **2024**, *9*, 726–735. [[CrossRef](#)] [[PubMed](#)]
- Xu, X.; Du, Q.; Kang, H.; Gu, X.; Shan, C.; Zeng, J.; Dai, T.; Yang, Q.; Sun, X.; Li, G.; et al. Uniform Molecular Adsorption Energy-Driven Homogeneous Crystallization and Dual-Interface Modification for High Efficiency and Thermal Stability in Inverted Perovskite Solar Cells. *Adv. Funct. Mater.* **2024**, *34*, 2408512. [[CrossRef](#)]
- Xie, Z.; Li, Y.; Li, X.; Fang, Y.; Chang, J.; Yang, Q.; Sun, X.; Miao, C.; Lu, G.; Chen, Z.; et al. High Performance Inverted Planar Perovskite Solar Cells Enhanced by Heteroatomic Functionalized Hole Transport Materials. *Mater. Chem. Front.* **2024**, *8*, 2764–2774. [[CrossRef](#)]
- Sun, X.; Fan, H.; Xu, X.; Li, G.; Gu, X.; Luo, D.; Shan, C.; Yang, Q.; Dong, S.; Miao, C.; et al. A Fluorination Strategy and Low-Acidity Anchoring Group in Self-Assembled Molecules for Efficient and Stable Inverted Perovskite Solar Cells. *Chem.-A Eur. J.* **2024**, *30*, e202400629. [[CrossRef](#)] [[PubMed](#)]
- Wang, C.; Hu, H.; Peng, D.; Dong, L.; Zhu, D. Soft devices empowered by mechanoluminescent materials. *Soft Sci.* **2023**, *3*, 39. [[CrossRef](#)]
- Li, G.; Liu, S.; Xu, Z.; Guo, J.; Tang, S.Y.; Ma, X. Recent advancements in liquid metal enabled flexible and wearable biosensors. *Soft Sci.* **2023**, *3*, 37. [[CrossRef](#)]
- Tang, G.; Mei, D.; Zhao, X.; Zhao, C.; Li, L.; Yanjie, W. A comprehensive survey of ionic polymer metal composite transducers: Preparation, performance optimization and applications. *Soft Sci.* **2023**, *3*, 9.
- Zhang, Z.; Zhao, D.; Xu, Y.; Liu, S.; Xu, X.; Zhou, J.; Gao, F.; Tang, H.; Wang, Z.; Wu, Y.; et al. A review on electrode materials of fast-charging lithium-ion batteries. *Chem. Rec.* **2022**, *22*, e202200127. [[CrossRef](#)]

9. Xiao, Y.; Wu, J.; Zhang, Y. Recent advances in the design, fabrication, actuation mechanisms and applications of liquid crystal elastomers. *Soft Sci.* **2023**, *3*, 11. [[CrossRef](#)]
10. Wang, X.; Qi, L.; Yang, H.; Rao, Y.; Chen, H. Stretchable synaptic transistors based on the field effect for flexible neuromorphic electronics. *Soft Sci.* **2023**, *3*, 15. [[CrossRef](#)]
11. Wei, X.; Liang, X.; Meng, C.; Cao, S.; Shi, Q.; Wu, J. Multimodal electronic textiles for intelligent human-machine interfaces. *Soft Sci.* **2023**, *3*, 17. [[CrossRef](#)]
12. Guess, M.; Soltis, I.; Rigo, B.; Zavanelli, N.; Kapasi, S.; Kim, H.; Yeo, W.-H. Wireless batteryless soft sensors for ambulatory cardiovascular health monitoring. *Soft Sci.* **2023**, *3*, 23. [[CrossRef](#)]
13. Wang, T.; He, J.; Zhu, Z.; Cheng, X.B.; Zhu, J.; Lu, B.; Wu, Y. Heterostructures Regulating Lithium Polysulfides for Advanced Lithium-Sulfur Batteries. *Adv. Mater.* **2023**, *35*, 2303520. [[CrossRef](#)] [[PubMed](#)]
14. Liu, W.D.; Tang, X.; Feng, J.A.; Zhang, C.Y.; Liu, H.; Shi, C.; Zhao, X.X.; Song, J.J. Recent advances in vacancy engineering for reliable lithium-sulfur batteries. *Rare Met.* **2024**, *43*, 455–477. [[CrossRef](#)]
15. Wang, Z.F.; Wang, H.Y.; Liu, X.L.; Chen, Y.X.; Zhao, Y.; Zhang, Y.G.; Han, Q.Q.; Qin, C.L.; Bakenov, Z.; Wang, Y.C.; et al. Single Zn atoms anchored on hollow carbon nanofiber network for dendrite-free lithium metal anode of flexible Li-S full cell. *Rare Met.* **2023**, *42*, 3705–3717. [[CrossRef](#)]
16. Zhao, D.; Jiang, S.; Yu, S.; Ren, J.; Zhang, Z.; Liu, S.; Liu, X.; Wang, Z.; Wu, Y.; Zhang, Y. Lychee seed-derived microporous carbon for high-performance sodium-sulfur batteries. *Carbon* **2023**, *201*, 864–870. [[CrossRef](#)]
17. Rao, X.Y.; Xiang, S.F.; Zhou, J.; Zhang, Z.; Xu, X.Y.; Xu, Y.Y.; Zhou, X.C.; Pan, Z.D.; Tan, S.C.; Dong, S.X.; et al. Recent progress and strategies of cathodes toward polysulfides shuttle restriction for lithium-sulfur batteries. *Rare Met.* **2024**, *43*, 4132–4161. [[CrossRef](#)]
18. Zhou, J.; Sun, S.; Zhou, X.; Rao, X.; Xu, X.; Zhang, Z.; Pan, Z.; Wang, Q.C.; Wang, Z.; Wu, Y.; et al. Defect engineering enables an advanced separator modification for high-performance lithium-sulfur batteries. *Chem. Eng. J.* **2024**, *487*, 150574. [[CrossRef](#)]
19. Song, M.; Liu, Y.; Hong, J.; Wang, X.; Huang, X. Boosting bidirectional conversion of polysulfide driven by the built-in electric field of MoS₂/MoP Mott-Schottky heterostructures in lithium-sulfur batteries. *J. Adv. Ceram.* **2023**, *12*, 1872–1888. [[CrossRef](#)]
20. Yang, W.H.; Ni, Z.C.; You, D.; Hou, J.Y.; Deng, B.N.; Huang, R.W.; Sun, S.G.; Zhao, J.B.; Li, X.; Zhang, Y.Y.; et al. Multifunctional sulfur-immobilizing GO/MXene aerogels for highly-stable and long-cycle-life lithium-sulfur batteries. *Rare Met.* **2023**, *42*, 2577–2591. [[CrossRef](#)]
21. Wen, Q.; Qu, F.; Yu, Z.; Graczyk-Zajac, M.; Xiong, X.; Riedel, R. Si-based polymer-derived ceramics for energy conversion and storage. *J. Adv. Ceram.* **2022**, *11*, 197–246. [[CrossRef](#)]
22. Liu, R.Q.; Jin, F.; Gu, M.; Zhang, D.W.; He, L.L.; Liu, W.X.; Zhu, W.F.; Xie, K.; Wu, J.Y.; Liu, Y.R.; et al. Titanium nitride nanorod array/carbon cloth as flexible integrated host for highly stable lithium-sulfur batteries. *Rare Met.* **2023**, *42*, 4115–4127. [[CrossRef](#)]
23. Liu, J.; Wei, A.; Pan, G.; Xiong, Q.; Chen, F.; Shen, S.; Xia, X. Atomic layer deposition-assisted construction of binder-free Ni@N-doped carbon nanospheres films as advanced host for sulfur cathode. *Nano-Micro Lett.* **2019**, *11*, 64. [[CrossRef](#)] [[PubMed](#)]
24. Liu, C.; Qiu, Y.; Liu, Y.; Xu, K.; Zhao, N.; Lao, C.; Shen, J.; Chen, Z. Novel 3D grid porous Li₄Ti₅O₁₂ thick electrodes fabricated by 3D printing for high performance lithium-ion batteries. *J. Adv. Ceram.* **2022**, *11*, 295–307. [[CrossRef](#)]
25. Gao, F.; Yue, X.A.; Xu, X.Y.; Xu, P.; Zhang, F.; Fan, H.S.; Wang, Z.L.; Wu, Y.T.; Liu, X.; Zhang, Y. A N/Co co-doped three-dimensional porous carbon as cathode host for advanced lithium-selenium batteries. *Rare Met.* **2023**, *42*, 2670–2678. [[CrossRef](#)]
26. Yin, C.; Li, Z.; Zhao, D.; Yang, J.; Zhang, Y.; Du, Y.; Wang, Y. Azo-branched covalent organic framework thin films as active separators for superior sodium-sulfur batteries. *ACS Nano* **2022**, *16*, 14178–14187. [[CrossRef](#)]
27. Zhang, Z.; Li, Y.; Cui, X.; Guan, S.; Tu, L.; Tang, H.; Li, Z.; Li, J. Understanding the advantageous features of bacterial cellulose-based separator in Li-S battery. *Adv. Mater. Interfaces* **2023**, *10*, 2201730. [[CrossRef](#)]
28. Liu, J.; Zhang, J.; Zhu, J.; Zhao, R.; Zhang, Y.; Ma, Y.; Li, C.; Zhang, H.; Chen, Y. A lithium sulfonylimide COF-modified separator for high-performance Li-S batteries. *Nano Res.* **2023**, *16*, 12601–12607. [[CrossRef](#)]
29. Yan, W.; Gao, X.; Jin, X.; Liang, S.; Xiong, X.; Liu, Z.; Wang, Z.; Chen, Y.; Fu, L.; Zhang, Y.; et al. Nonporous gel electrolytes enable long cycling at high current density for lithium-metal anodes. *ACS Appl. Mater. Interfaces* **2021**, *13*, 14258–14266. [[CrossRef](#)]
30. Zhou, Y.; Yin, L.; Xiang, S.; Yu, S.; Johnson, H.M.; Wang, S.; Yin, J.; Zhao, J.; Luo, Y.; Chu, P.K. Unleashing the potential of MXene-based flexible materials for high-performance energy storage devices. *Adv. Sci.* **2024**, *11*, 2304874. [[CrossRef](#)]
31. Pan, Z.; Yu, S.; Wang, L.; Li, C.; Meng, F.; Wang, N.; Zhou, S.; Xiong, Y.; Wang, Z.; Wu, Y.; et al. Recent advances in porous carbon materials as electrodes for supercapacitors. *Nanomaterials* **2023**, *13*, 1744. [[CrossRef](#)] [[PubMed](#)]
32. Anasori, B.; Xie, Y.; Beidaghi, M.; Lu, J.; Hosler, B.C.; Hultman, L.; Kent, P.R.C.; Gogotsi, Y.; Barsoum, M.W. Two-dimensional, ordered, double transition metals carbides (MXenes). *ACS Nano* **2015**, *9*, 9507. [[CrossRef](#)] [[PubMed](#)]
33. Guo, Y.; Zhang, X.; Jin, S.; Xia, Q.; Chang, Y.; Wang, L.; Zhou, A. Synthesis of Mo₂C MXene with high electrochemical performance by alkali hydrothermal etching. *J. Adv. Ceram.* **2023**, *12*, 1889–1901. [[CrossRef](#)]
34. Mou, J.; Li, S.; Zhang, W.; Xu, W.; Fan, S.; Bei, G. Deintercalation of Al from MoAlB by molten salt etching to achieve a Mo₂AlB₂ compound and 2D MoB nanosheets. *J. Adv. Ceram.* **2023**, *12*, 943–953. [[CrossRef](#)]
35. Wang, A.; Chen, Y.; Liu, L.; Liu, X.; Wang, Z.; Zhang, Y. Sulfur nanoparticles/Ti₃C₂Tx MXene with an optimum sulfur content as a cathode for highly stable lithium-sulfur batteries. *Dalton Trans.* **2021**, *50*, 5574–5581. [[CrossRef](#)]
36. Yao, Y.; Feng, W.; Chen, M.; Zhong, X.; Wu, X.; Zhang, H.; Yu, Y. Boosting the electrochemical performance of Li-S batteries with a dual polysulfides confinement strategy. *Small* **2018**, *14*, 1802516. [[CrossRef](#)]

37. Huang, Y.; Yang, H.; Zhang, Y.; Zhang, Y.; Wu, Y.; Tian, M.; Chen, P.; Trout, R.; Ma, Y.; Wu, T.H.; et al. A safe and fast-charging lithium-ion battery anode using MXene supported Li₃VO₄. *J. Mater. Chem.* **2019**, *7*, 11250–11256. [[CrossRef](#)]
38. Fang, B.; Tian, X.; Wang, T.; Wang, T.; Qu, L.; Li, M. Restraining Polysulfide with High-Entropy Metal Nitride towards Long Cycle Life and High Capacity Li-S Batteries. *ChemElectroChem* **2020**, *7*, 4737–4744. [[CrossRef](#)]
39. Ma, G.; Wen, Z.; Jin, J.; Lu, Y.; Rui, K.; Wu, X.; Wu, M.; Zhang, J. Enhanced performance of lithium sulfur battery with polypyrrole warped mesoporous carbon/sulfur composite. *J. Power Sources* **2014**, *254*, 353–359. [[CrossRef](#)]
40. Qiu, Y.; Li, W.; Zhao, W.; Li, G.; Hou, Y.; Liu, M.; Zhou, L.; Ye, F.; Li, H.; Wei, Z.; et al. High-rate, ultralong cycle-life lithium/sulfur batteries enabled by nitrogen-doped graphene. *Nano Lett.* **2014**, *14*, 4821–4827. [[CrossRef](#)]
41. Zhang, J.; Xiang, J.; Dong, Z.; Liu, Y.; Wu, Y.; Xu, C.; Du, G. Biomass derived activated carbon with 3D connected architecture for rechargeable lithium–sulfur batteries. *Electrochim. Acta* **2014**, *116*, 146–151. [[CrossRef](#)]
42. Wang, H.; Yang, Y.; Liang, Y.; Robinson, J.T.; Li, Y.; Jackson, A.; Cui, Y.; Dai, H. Graphene-wrapped sulfur particles as a rechargeable lithium–sulfur battery cathode material with high capacity and cycling stability. *Nano Lett.* **2011**, *11*, 2644–2647. [[CrossRef](#)] [[PubMed](#)]
43. Niu, H.; Jiang, X.; Xia, Y.; Wang, H.; Zhang, R.; Li, H.; Fan, B.; Zhou, Y. Construction of hydrangea-like core–shell SiO₂@Ti₃C₂T_x@CoNi microspheres for tunable electromagnetic wave absorbers. *J. Adv. Ceram.* **2023**, *12*, 711–723. [[CrossRef](#)]
44. Cai, Z.; Ma, Y.F.; Wang, M.; Qian, A.-N.; Tong, Z.; Xiao, L.; Jia, S.; Chen, X. Engineering of electrolyte ion channels in MXene/holey graphene electrodes for superior supercapacitive performances. *Rare Met.* **2022**, *41*, 2084–2093. [[CrossRef](#)]
45. Xia, Y.Y.; Deng, S.L.; Sun, X.Z.; Li, B.; Chen, J. Progress of symmetrical solid oxide fuel cell. *Adv. Ceram.* **2023**, *44*, 129–141.
46. Xu, H.; Zheng, R.; Du, D.; Ren, L.; Wen, X.; Wang, X.; Tian, G.; Shu, C. Adjusting the 3d Orbital Occupation of Ti in Ti₃C₂ MXene via Nitrogen Doping to Boost Oxygen Electrode Reactions in Li-O₂ Battery. *Small* **2023**, *19*, 2206611. [[CrossRef](#)]
47. Liu, W.; Cao, J.; Song, F.; Zhang, D.D.; Okhawilai, M.; Yi, J.; Qin, J.Q.; Zhang, X.Y. A double transition metal Ti₂NbC₂T_x MXene for enhanced lithium-ion storage. *Rare Met.* **2023**, *42*, 100–110. [[CrossRef](#)]
48. Jiang, T. Fabrication technology, research and development status, development trend of the ternary laminated structure MAX phase ceramics materials. *Adv. Ceram.* **2023**, *44*, 1–23.
49. Sun, Z.; Hu, Y.; Zhang, J.; Zhou, N.; Li, M.; Liu, H.; Huo, B.; Chao, M.; Zeng, K. Interfacial oxygen bridge bonding with Mo-O-Ti units in MoOx@ Ti₃C₂ MXene harness efficient Li-O₂ Battery at high rate. *Appl. Catal. Environ. Energy* **2024**, *351*, 123984. [[CrossRef](#)]

Disclaimer/Publisher’s Note: The statements, opinions and data contained in all publications are solely those of the individual author(s) and contributor(s) and not of MDPI and/or the editor(s). MDPI and/or the editor(s) disclaim responsibility for any injury to people or property resulting from any ideas, methods, instructions or products referred to in the content.